Anthropogenic Aerosols Dominate Forced Multidecadal Sahel Precipitation Change through Distinct Atmospheric and Oceanic Drivers

HARUKI HIRASAWA AND PAUL J. KUSHNER

Department of Physics, University of Toronto, Toronto, Ontario, Canada

MICHAEL SIGMOND AND JOHN FYFE

Canadian Centre for Climate Change Modelling and Analysis, Environment and Climate Change Canada, Victoria, British Columbia, Canada

CLARA DESER

National Center for Atmospheric Research, Boulder, Colorado

(Manuscript received 1 November 2019, in final form 24 August 2020)

ABSTRACT: Sahel precipitation has undergone substantial multidecadal time scale changes during the twentieth century that have had severe impacts on the region's population. Using initial-condition large ensembles (LE) of coupled general circulation model (GCM) simulations from two institutions, forced multidecadal variability is found in which Sahel precipitation declines from the 1950s to 1970s and then recovers from the 1970s to 2000s. This forced variability has similar timing to, but considerably smaller magnitude than, observed Sahel precipitation variability. Isolating the response using single forcing simulations within the LEs reveals that anthropogenic aerosols (AA) are the primary driver of this forced variability. The roles of the *direct-atmospheric* and the *ocean-mediated* atmospheric responses to AA forcing are determined with the atmosphere–land GCM (AGCM) components of the LE coupled GCMs. The direct-atmospheric response arises from changes to aerosol and precursor emissions with unchanged oceanic boundary conditions while the ocean-mediated response arises from changes to AA-forced sea surface temperatures and sea ice concentrations diagnosed from the AA-forced LE. In the AGCMs studied here, the direct-atmospheric response dominates the AA-forced 1970s − 1950s Sahel drying. On the other hand, the 2000s − 1970s wetting is mainly driven by the ocean-mediated effect, with some direct atmospheric contribution. Although the responses show differences, there is qualitative agreement between the AGCMs regarding the roles of the direct-atmospheric and ocean-mediated responses. Since these effects often compete and show nonlinearity, the model dependence of these effects and their role in the net aerosol-forced response of Sahel precipitation need to be carefully accounted for in future model analysis.

KEYWORDS: Africa; Monsoons; Aerosols; Atmosphere-ocean interaction; General circulation models; Multidecadal variability

1. Introduction

Emissions of anthropogenic aerosols (AAs) and their chemical precursors have undergone spatially and temporally complex variations that present an intriguing challenge for understanding anthropogenic influence on multidecadal climate variability. One climate variability signal that has been linked to AA forcing is twentieth-century multidecadal variability of Sahel precipitation, which featured a wet period in the 1950s, drought conditions that peaked in the 1980s, and a moderate recovery thereafter toward the present day (e.g., Dai et al. 2004; Rodríguez-Fonseca et al. 2015). The coincident timing of Sahel precipitation with variations of sulfur dioxide emissions from North America and Europe suggests a potential causal link between these precipitation changes and AA forcing. Indeed, the drying effect of AA forcing on the Sahel has been well established in general circulation models (GCMs) (Rotstayn and Lohmann 2002; Held et al. 2005; Kawase et al. 2010; Ackerley et al. 2011; Westervelt et al. 2017; Undorf et al. 2018; Hua et al. 2019). For example, Undorf et al. (2018) detected a signature of AA forcing on twentieth-century West African precipitation variability using an ensemble of CMIP5 models, but also found that the model responses needed to be scaled up to match observations. Uncertainty remains regarding the extent of anthropogenic influence on Sahel precipitation due to the inability of GCMs to capture the region's climatology and variability (Giannini et al. 2008; Biasutti 2019) and due to uncertainty in AA forcing and its forced impact on the climate (Myhre et al. 2013).

Proposed mechanisms of climate change can be generally be categorized into two broad pathways: 1) *direct-atmospheric* pathways that comprise rapid atmospheric responses to radiative and cloud impacts of an external forcing and 2) *ocean-mediated* pathways that comprise atmospheric responses to ocean surface anomalies due to internal and externally forced

Supplemental information related to this paper is available at the Journals Online website: https://doi.org/10.1175/JCLI-D-19-0829.s1.

Corresponding author: Haruki Hirasawa, hirasawa@physics.utoronto.ca

DOI: 10.1175/JCLI-D-19-0829.1

variability. [We prefer this "direct-atmospheric"/"ocean-mediated" terminology to the ambiguous "fast"/"slow" terminology (e.g., Andrews et al. 2009; Biasutti 2013; Li et al. 2018) since rates of climate response to external forcing can range from weeks to millennia.]

Determining the roles of direct-atmospheric versus ocean-mediated mechanisms has been central to understanding the drivers of the late-twentieth-century Sahel drought. Charney (1975) hypothesized that the observed Sahel drought was a direct-atmospheric response to increasing surface albedo from overgrazing in the region. Although land cover changes are important for understanding climate changes in the region, such as the Green Sahara period (e.g., Braconnot et al. 1999; Pausata et al. 2016), overgrazing is insufficient to account for the twentieth-century drought (Biasutti 2019). Further work instead found that Sahel precipitation variability, and the twentieth-century drought in particular, is predominantly a response to large-scale variations in global sea surface temperature (SST) (Lamb 1978; Folland et al. 1986; Palmer 1986), a view that has come to be widely accepted in the field (Giannini et al. 2008; Rodríguez-Fonseca et al. 2015; Biasutti 2019).

Decomposing Sahel climate change into its direct-atmospheric and ocean-mediated components highlights the complexities of the region's response to external radiative forcing. The two components of the response to greenhouse gas (GHG) forcing tend to have opposing effects on Sahel precipitation, exacerbating uncertainties in projected future changes for the region (Biasutti 2013; Gaetani et al. 2017). Furthermore, Dong and Sutton (2015) found that much of the precipitation recovery since the 1980s is due to the direct-atmospheric response to GHGs. In the case of AA forcing, the Sahel precipitation response to increasing AA forcing is often interpreted as a primarily ocean-mediated response. AA forcing is thought to cause Sahel drying by cooling the North Atlantic relative to the South Atlantic, shifting the intertropical convergence zone southward (Ackerley et al. 2011; Mohino et al. 2011; Hwang et al. 2013; Wang 2015; Hua et al. 2019; Bonfils et al. 2020), or by cooling the North Atlantic relative to the global tropical ocean, reducing the West African monsoon's ability to supply sufficient heat and moisture to meet the threshold for convection (Giannini et al. 2013; Giannini and Kaplan 2019). However, studies of atmosphere–land GCM (AGCM) simulations have also found that there is a direct-atmospheric Sahel drying response to AAs even in the absence of an ocean-mediated response (Dong et al. 2014; Richardson et al. 2016). Furthermore, studies of the Asian monsoon have also found that AA forcing causes direct-atmospheric and ocean-mediated responses that have different, and in places competing, roles in regional precipitation changes (Ganguly et al. 2012; Li et al. 2018). Thus, there is a need to study these components of the response together to assess their relative contributions to the AA-forced effect on past Sahel drought.

We seek here to robustly characterize the climate response of Sahel precipitation to AA forcing since the 1950s, and to identify the roles of direct-atmospheric and ocean-mediated responses in the coupled response. We take a two-part approach. First, we examine historical climate variability in initial condition large ensembles (LEs) from two independently developed coupled GCMs. Subsets of these large ensembles are forced by different combinations of external forcing agents. Using different combinations of radiative forcing allows us to identify the effects of individual forcing agents; using LEs allows us to do so in a way that separates forced signals from internal variability; and using independent GCMs allows us to examine whether forced signals so obtained are robust between the models. In particular, we aim to isolate the role of AAs in the externally forced response of Sahel precipitation in the historic period. Second, we conduct AGCM experiments focused on three epochs in the latter half of the twentieth century, with the AGCM components of the coupled GCMs used for the LEs. We choose three epochs that enable us to partially resolve the increase and subsequent decline of AA emissions from regions like North America and Europe. The AA-forced SST and sea ice concentration (SIC) anomalies from the LEs are used to perturb oceanic boundary conditions for the AGCM experiments. The use of LEs is critical, as the patterned SST response to AA forcing can be relatively weak and thus obscured by internal variability (Oudar et al. 2018). These experiments allow us to investigate the roles of the direct-atmospheric and ocean-mediated responses in AA-forced multidecadal variability of Sahel precipitation since the 1950s. Here again, we will be able to compare the AGCM responses in two separate models to get a sense of the robustness to model formulation.

Section 2 provides details on the large ensemble coupled GCM and the AGCM simulations analyzed in this study. In section 3, we analyze the LE simulations and the coupled climate response to AA forcing in the Sahel. In section 4, we analyze the AGCM simulations and the resultant direct-atmospheric and ocean-mediated responses. Concluding remarks are made in section 5.

2. Methods

a. *Coupled general circulation model large ensemble simulations*

We use large initial condition ensembles (LE) of coupled ocean–atmosphere GCM simulations from the National Center for Atmospheric Research–Department of Energy Community Earth System Model 1 (NCAR–DOE CESM1) (Kay et al. 2015) and the Canadian Centre for Climate Modeling and Analysis Canadian Earth System Model 2 (CCCma CanESM2) (Kirchmeier-Young et al. 2017; Kushner et al. 2018). Aerosol levels in both models are set by prescribing emissions of aerosols (e.g., black carbon) and aerosol precursors (e.g., sulfur dioxide) of anthropogenic origin. The simulations used in this study are summarized in Table 1.

In addition to the original historical forcing LE simulations, there are LE simulations in both models that are configured to isolate the effects of AA forcing. From the CESM1 LE we analyze 35 all-forcing (ALL) and 20 all-but-aerosol forcing (XAER) simulations that are carried out at a nominal 1° resolution (Deser et al. 2020). In the XAER simulation, external forcings follow their historical trajectory except for industrial AA and their precursor emissions, which are held fixed to 1920 conditions (Deser et al. 2020). Notably, biomass burning (BMB)

TABLE 1. A summary of the coupled ocean–atmosphere GCM simulations used in this study.

Model	Simulation name	Anthropogenic aerosol emissions	Biomass burning emissions	Other external forcings	N	Years
CESM1	ALL	Historical	Historical	Historical	35	1920–2080
CESM1	XAER	1920	Historical	Historical	20	1920–2080
CESM1	XBMB	Historical	1920	Historical	15	1920–2029
CESM1	AER	Historical	Historical	Pre-industrial	3	1850–2005
CanESM2	ALL	Historical	Historical	Historical	50	1950–2020
CanESM2	AER	Historical	Historical	Pre-industrial	50	1950–2020

aerosol emissions are not grouped with AA in the XAER simulations. Thus, we also analyze a set of 15 all-but-biomass burning aerosol (XBMB) simulations from the CESM1 LE to assess the impact of BMB aerosols. These simulations are analogous to the XAER simulations, but for BMB aerosol emissions. The impact of AA forcing is determined by taking the difference of the ensemble mean of the ALL minus the XAER simulations. To obtain the ensemble spread of "aerosol only" simulations for CESM1, individual AER ensemble members are calculated as

$$\mathrm{AER}_i = (\mathrm{XAER}_i - \mathrm{XAER}_{\mathrm{em}}) + (\mathrm{ALL}_{\mathrm{em}} - \mathrm{XAER}_{\mathrm{em}}),$$

where subscript i denotes an individual ensemble member and subscript "em" denotes the ensemble mean (Deser et al. 2020).

From the CanESM2 LE we analyze 50 all forcing (ALL) simulations and 50 AA-only simulations (AER) that are carried out at T63 resolution (~2° resolution). In contrast to the XAER simulations, in the AER simulations AAs and their precursor emissions vary along their historical trajectories while all other external forcings are set to preindustrial conditions. Unlike the CESM1 LE, BMB aerosol emissions are included with industrial AAs in the CanESM2 LE AER simulations.

Both the ALL and the XAER LEs in CESM1 were initialized using round-off level atmospheric perturbations from a single all-forcing historical simulation at 1920. The latter was in turn initialized at 1850 from a long 1850 control integration (Kay et al. 2015; Pendergrass et al. 2019; Deser et al. 2020). As a result, all the simulations in the CESM1 ALL and XAER ensembles have the same ocean conditions at their initialization in 1920. The ALL and AER CanESM2 LE simulations are initialized by using atmospheric perturbations to branch 10 simulations at 1950 from each simulation in two smaller five-member ALL and AER forcing ensembles. These original simulations are initialized at 1850 by randomly sampling ocean–atmosphere states from a preindustrial control simulation (Kirchmeier-Young et al. 2017; Kushner et al. 2018).

If the forced responses to different external forcings were approximately additive, the two simulation protocols for isolating the response to AA would be approximately equivalent. We partially test for nonadditivity using a small three-member ensemble of historical AER simulations in CESM1. Note that the emission changes differ in the two CESM1 ensembles, as BMB aerosols are included in the small aerosol-only CESM1 ensemble (Table 1). Additionally, the three-member ensemble was conducted in the CMIP5 CESM1-CAM5 version of CESM1, which differs slightly from the CESM1-LE version (Kay et al. 2015).

Precipitation variability in the LEs are evaluated against the Global Precipitation Climatology Centre precipitation analysis (Schneider et al. 2015), the Climate Research Unit Time series (CRU TS) (University of East Anglia Climatic Research Unit 2013), the University of Delaware Terrestrial Precipitation (U. Delaware) (Willmott and Matsuura 2001), and the National Oceanic and Atmospheric Administration Precipitation Reconstruction over Land (PREC/L) (Chen et al. 2002). Further analysis is conducted comparing a set of transient AGCM simulations from CAM5 to CESM1 and CanAM4 to CanESM2 in which SST/SIC conditions are set to their historical observed conditions and external forcing agents vary along their historical trajectories. For CanAM4 we analyze four AMIP simulations carried out from 1950 to 2009 (von Salzen et al. 2013). For CAM5 we analyze 50 C20C+ simulations carried out from 1959 to 2012 (Stone et al. 2018). Note that aerosol levels are prescribed by concentration in the CAM5 C20C+ simulations rather than by emissions as in CESM1 and the CAM5 AGCM simulations described below.

Both CESM1 and CanESM2 include prognostic aerosol schemes that differ in their representation of aerosol processes such as formation, deposition, and cloud interactions. CESM1 uses the Modal Aerosol Model version 3 (Liu et al. 2012) and includes representations of both the aerosol–cloud albedo (Twomey 1977) and aerosol–cloud lifetime effects (Neale et al. 2012). CanESM2 uses a bulk aerosol model and only represents the aerosol-cloud albedo effect (von Salzen et al. 2013). This results in differing aerosol effective radiative forcings (ERFs) with CESM1 at $-1.37\,\mathrm{W\,m^{-2}}$ and CanESM2 at $-0.84\,\mathrm{W\,m^{-2}}$ (Zelinka et al. 2014). It has been found that CESM1 overestimates the enhancement of cloud liquid water path in response to aerosol perturbations from naturally occurring tropospheric volcanic aerosols (Malavelle et al. 2017), which suggests the model may overestimate the negative radiative forcing due to the aerosol–cloud lifetime effect (Toll et al. 2019). CESM1-CAM5 and CanESM2 were identified in Monerie et al. (2017) as having similar patterns of Sahel -precipitation response to projected GHG forcing. However, as GHG radiative forcing largely affects the longwave and the spatial patterns of the GHG and AA forcings differs, this finding does not necessarily apply to the historical response to AA forcing.

We focus our analysis and additional simulations on three periods during the late twentieth century: 1950–59 (1950s),

TABLE 2. Descriptions of the CAM5 and CanAM4 AA and precursor emission and SST/SIC conditions in the AGCM simulations. The 2000s climatological SST/SIC were obtained from the HadISST dataset.

Expt	Anthropogenic aerosol emissions	SST/sea ice	Years	
			CAM5	CanAM4
1	2000s	2000s	100	100
2	1970s	2000s	100	100
3	2000s	2000s + (1970s–2000s SST/sea ice from LENS)	50	100
4	1970s	2000s + (1970s–2000s SST/sea ice from LENS)	50	100
5	1950s	2000s	100	100
6	2000s	2000s + (1950s–2000s SST/sea ice from LENS)	50	100
7	1950s	2000s + (1950s–2000s SST/sea ice from LENS)	50	100

1970–79 (1970s), and 2000–09 (2000s). The 1950–59 period is the initial decade of the CanESM2 LE simulations and represents a time of relatively weak AA forcing and high Sahel precipitation. The 1970–79 period marks the peak of sulfur dioxide emissions in North America and Europe (NA/EU), and thus strong sulfate AA forcing in those regions (Smith et al. 2011). Sulfur dioxide emissions in these regions subsequently declined due to air quality regulations toward the near present-day 2000–09 period while emissions from Asia continued to increase. Thus, we study two distinct regimes in the history of sulfur dioxide emissions (and thus sulfate aerosol burdens): 1) the 1970s minus the 1950s (drying period), which is a period of drying in the Sahel region along with strong increases in AA-related emissions from NA/EU and moderate increases from Asia; 2) and the 2000s minus the 1970s (recovery period), which is a period of precipitation recovery in the Sahel along with a decline in emissions from NA/EU and continued emissions increases from Asia.

b. *Atmospheric general circulation model simulation*

To separate the roles of the direct-atmospheric response and the ocean-mediated response in the total coupled response to AA forcing we perform a set of "time-slice" AGCM experiments using the atmospheric and land components of the LE models: the Community Atmosphere Model version 5 (CAM5) for CESM1 (Neale et al. 2012) and the Canadian Atmosphere Model version 4 (CanAM4) for CanESM2 (von Salzen et al. 2013). Time-slice AGCM simulations use boundary conditions that vary seasonally, but do not vary from year to year. The simulation descriptions are summarized in Table 2. Similar protocols have been used in Ganguly et al. (2012) and Li et al. (2018) to study the Asian monsoon response to AA forcing. The simulations described here provide two advantages over previous work:

- They provide more information about the multidecadal evolution of the precipitation signal by comparing three decades rather than the effect of change between two epochs such as the preindustrial to present-day change.
- They utilize initial condition large ensembles to filter internal climate variability in SST and sea ice. Thus, by applying these anomalies as perturbations to the atmosphere components of the coupled models, it is possible to obtain model-consistent estimates of the direct-atmospheric and ocean-mediated responses such that the AGCM simulations approximate the response from their respective coupled LE simulations.

The control simulation (Exp 1) is set to seasonally varying observed conditions averaged over 2000–09 globally, with the SST and sea ice concentration climatology calculated using the Hadley Centre Global Sea Ice and Sea Surface Temperature dataset (Rayner et al. 2003). AA emissions are averaged over 2000–09 with data pre-2005 using historical emissions and post-2005 using RCP8.5 projected emissions. Other forcing conditions, such as GHG and land use, are set to year 2000 conditions. We then perturb the boundary conditions away from this control simulation and obtain the response of the 2000s − 1970s (2000s − 1950s) by changing aerosol emissions in Exp 2 (Exp 5), perturbing the SST/SIC conditions using AA-forced LE anomalies in Exp 3 (Exp 6), or applying both changes in Exp 4 (Exp 7). The response for the 1970s − 1950s is then calculated as the difference between the 2000s − 1950s and 2000s − 1970s responses and thus is noisier than the 2000s − 1970s response.

In the AGCM simulations, the direct-atmospheric response is obtained by modifying the aerosol and aerosol precursor emissions to the levels of the target decade. For CAM5, we do not modify BMB aerosol emissions as they are not included with industrial AA emissions in the CESM1 LE XAER simulations. For CanAM4, BMB aerosol emissions are included as they are also included in the CanESM2 LE AER simulations. The boundary conditions for the AGCM simulations that provide the ocean-mediated response are obtained by calculating the ensemble and time mean SST and SIC anomalies due to AA forcing in the coupled LEs for each month of the year for the 2000s minus the target decade, then subtracting these anomalies from the observed climatology. The SST and SIC fields are then adjusted in sea ice regions to ensure physical consistency between the two fields (Hurrell et al. 2008). Sea ice thickness is not modified in these simulations.

By using the anomalies from each set of LE simulations as perturbations in their respective atmosphere components, we obtain a combined direct-atmospheric plus ocean-mediated response that is, in principle, equivalent to the total coupled response of the LE simulations. However, the match between the AGCM and coupled simulations will be imperfect due to missing feedbacks from the lack of ocean–atmosphere coupling in the AGCM experiments, the use of time-slice rather than transient forcing, and the nonadditive or state-dependent effects introduced by the construction of the SST/SIC boundary forcing (in which perturbations are applied to the observed SST/SIC climatology rather than the model climatology, which

would provide a cleaner comparison to the coupled results). The ability of the AGCM experiments to replicate the LE response is evaluated in section 4a.

The two boundary condition perturbations are applied separately and combined in both models for the 2000s minus 1950s and 2000s minus 1970s giving a total of seven time-slice simulations (including the control) for each model which are each at least 50 years in length (Table 2). The direct-atmospheric and ocean-mediated responses can be calculated in two ways (Table S1 in the online supplemental material). For example, if we consider the direct-atmospheric response for the 2000s − 1970s, it can be calculated as EXP 1 minus EXP 2 in which we change AA emissions with a background of control SST/SIC (CTRL SST), as well as EXP 3 minus EXP 4 in which we change AA emissions with a background of SST/SIC perturbed with the AA-forced anomalies (PERT SST). Thus, we obtain the direct-atmospheric response with two different SST/SIC background conditions. Similarly, the ocean-mediated response can be obtained with control (CTRL EMIS) or perturbed (PERT EMIS) AA emissions. We evaluate the nonlinearity in the AGCM responses by comparing different combinations of simulations in section 4. However, for Figs. 6–11 (shown later) both combinations are averaged together in order to maximize the statistical sampling of the responses. The full list of combinations used is listed in Table S1.

c. *Moisture budget analysis*

Analysis of the atmospheric moisture budget is conducted following the moisture convergence (MC) method of Li and Ting (2017), wherein a detailed derivation of the following equations can be found. The steady state balance of atmospheric moisture is approximated as

$$\Delta(P-E) \approx \delta\mathrm{MC} + \delta\mathrm{ED} = \delta\mathrm{TH} + \delta\mathrm{DY} + \delta\mathrm{ED},$$

where precipitation P minus evaporation E anomaly is approximated as the sum of a mean flow (δMC) and an eddy (δED) component of the moisture convergence change, with the mean flow component further divided into the mean flow thermodynamic (δTH) and dynamic (δDY) terms. These two terms are calculated as

$$\delta\mathrm{TH} + \delta\mathrm{DY} = \frac{-1}{g\rho_w}\nabla\cdot\sum_{k=1}^{K}\mathbf{u}_{k,C}\delta q_k \Delta p_k - \frac{1}{g\rho_w}\nabla\cdot\sum_{k=1}^{K}\delta\mathbf{u}_k q_{k,C}\,\Delta p_k,$$

with gravitational acceleration g, density of water ρ_w, vertical pressure level k, total vertical levels K, pressure thickness of level k Δp_k, horizontal wind vector at level k $\mathbf{u_k}$, and specific humidity at level k q_k. All variables represent the climatological average of monthly mean values, $()_C$ indicates the time-averaged value in the control simulation and the δ symbol indicates the response calculated as $\delta() = ()_F - ()_C$, where $()_F$ is the time-averaged value in the perturbed simulation.

In these equations, responses to different forcings in the long-term mean of the time-slice AGCM simulations are interpreted as anomalies with respect to a control climatology. The mean flow thermodynamic term (δTH) represents the contribution of anomalous specific humidity (δq) being advected by the climatological winds ($\mathbf{u}_C$) and the mean flow dynamic term (δDY) represents the contribution of anomalous winds ($\delta\mathbf{u}$) advecting the climatological specific humidity (q_C). We calculate δTH and δDY and assume the residual between these two terms and the $P - E$ is dominated by the δED term, thus neglecting the quadratic term associated with covarying $\mathbf{u}$ and q anomalies. That is, products of the response are neglected in this simple budget.

3. Coupled GCM large ensemble responses

July–September (JAS) precipitation over the Sahel undergoes significant forced multidecadal changes over the late twentieth century in CESM1 (Fig. 1) and CanESM2 (Fig. 2) LEs. In both models, the ensemble mean of the ALL forcing simulations exhibits a JAS drying across much of Northern Hemisphere Africa in the drying period (1970s − 1950s) (Figs. 1a and 2a) and a wetting over the Sahel and drying over the Guinea coast in the recovery period (2000s − 1970s) (Figs. 1c and 2c). Comparison of the ALL forcing ensembles to the AA forcing simulations shows a close correspondence between the response to ALL and AA forcings. This indicates that AA forcing is the predominant cause of the 1970s − 1950s forced drying (Figs. 1b and 2b) and a substantial contributor to the 2000s − 1970s forced recovery (Figs. 1d and 2d). The ALL forcing response sees larger increases in precipitation compared to the AA forcing response in the recovery period in both models, suggesting that strengthening GHG forcing contributes to the recovery of precipitation, as discussed in previous studies (e.g., Dong and Sutton 2015; Giannini and Kaplan 2019). This GHG effect on the recovery is stronger in CanESM2 (Fig. 2c vs Fig. 2d) than in CESM1 (Fig. 1c vs Fig 1d), especially in the Sahel. Both models simulate similar patterns of precipitation response to AA forcing over the region, although the local maximum of the CanESM2 response occurs south of the Sahel. Analysis of the signal to noise of the precipitation change suggests that the minimum ensemble size required to detect a statistically significant response to AA forcing using the t test requires as many as 20 ensemble members over much of the Sahel for the 1970s − 1950s (Fig. S1), reinforcing the need for LEs to identify forced signals on multidecadal time scales.

The transient behavior of this climate signal is shown in Fig. 3, which displays the 11-yr moving average of JAS precipitation averaged over the Sahel (10°–20°N, 20°W–35°E excluding ocean grid points; see the blue boxes in Figs. 1a,b and 2a,b). There is close correspondence of the ALL and AER ensemble means in both CESM1 (Fig. 3a) and CanESM2 (Fig. 3b) with a good degree of agreement between the two coupled GCMs in the timing and amplitude of the forced variability. CanESM2 has relatively small intraensemble variability compared to CESM1 in this region, which is in part due to the largest precipitation anomalies occurring south of the Sahel in CanESM2 (Fig. 2). This in turn may be due to the latitudinal peak of climatological precipitation over Africa occurring further south in CanESM2 relative to CESM1 (Fig. S2). The dominance of AA forcing in the externally forced variability seen here is consistent with the analysis of Undorf et al. (2018), who detected an AA-forced signal in West

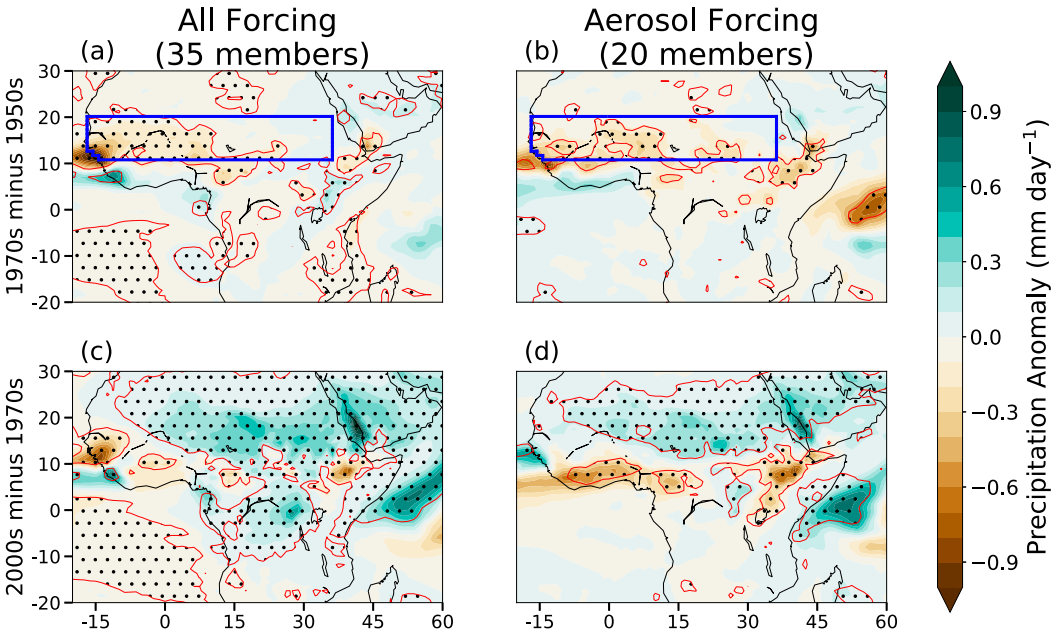

FIG. 1. Ensemble mean JAS precipitation anomalies from the CESM1 large ensemble simulations for the (top) 1970s − 1950s and (bottom) 2000s − 1970s in (a),(c) CESM1 ALL and (b),(d) ALL-XAER. Stippling surrounded by a thin red contour indicates grid points whose responses are statistically significant at the 95% level. The blue box indicates the averaging region used in Figs. 3 and 12, which includes notches on the western edge as a result of masking out ocean grid boxes.

African monsoon precipitation in the CMIP5 multimodel ensemble. The CanESM2 ALL and AER ensemble means diverge somewhat in the 2000s, suggesting an increased wetting effect due to GHG. Nonetheless, AA forcing has the largest contribution to the recovery in both models, in contrast to the findings of Dong and Sutton (2015) who saw a dominant role of the direct-atmospheric response to GHG in the recovery of Sahel precipitation in their AGCM simulations. In CESM1, the AA forcing response drives a -0.14 mm day^{-1} drying for the 1970s − 1950s and a 0.13 mm day^{-1} wetting for the 2000s − 1970s.

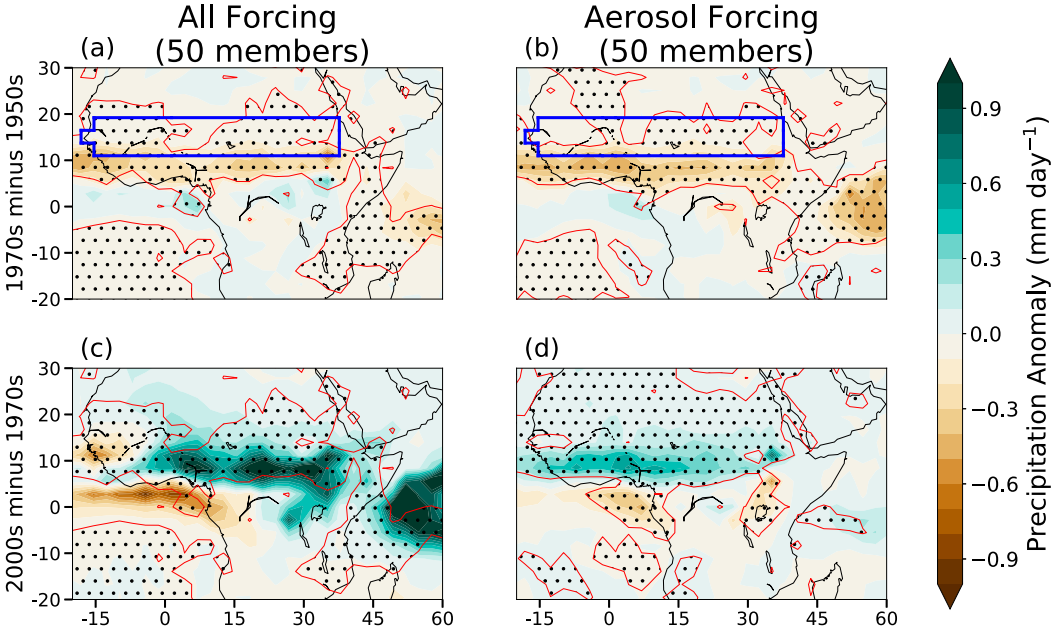

FIG. 2. As in Fig. 1, but for the CanESM2 large ensemble's (a),(c) ALL and (b),(d) AER simulations.

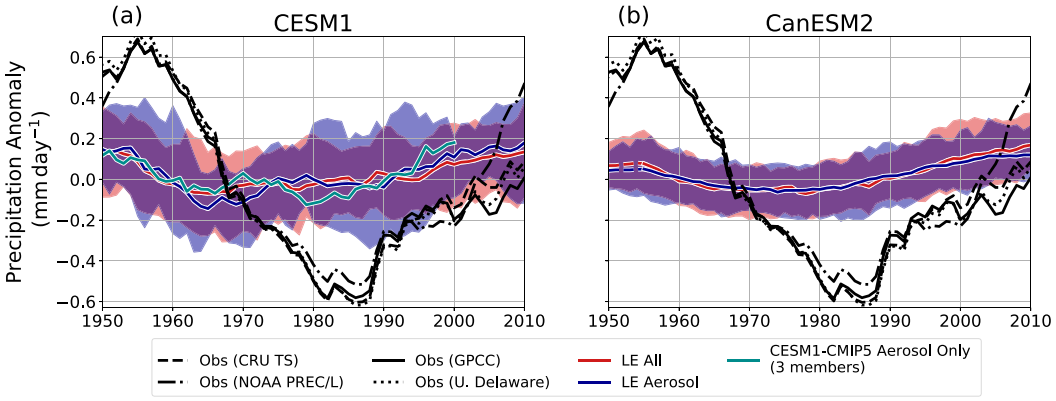

FIG. 3. The 11-yr central moving average Sahel regional average July–September (JAS) precipitation anomalies relative to the 1950–99 mean (10°–20°N and 20°W–35°E, excluding ocean grid points) from the (a) CESM1 and (b) CanESM2 large ensembles. The ensemble means of the LEs are shown in solid red (all forcing response) and blue (AA forcing response) lines where the AA forcing response is calculated as the ensemble mean of ALL-XAER for CESM1 and ensemble mean of AER CanESM2. Shading indicates the 5th–95th percentile ranges of each large ensemble. The ensemble mean of a smaller three-member ensemble of AA-only simulations in CESM1-CMIP5 (cyan) is plotted in (a). The 11-yr central moving average observed JAS precipitation anomalies from CRU TS (dashed), NOAA PREC/L (dash-dotted), GPCC (solid), and U. Delaware (dotted) are overlaid on the modeled anomalies in black.

As a fraction of the ALL forcing response, these are 118% and 102% of the forced response in their respective periods. In CanESM2, the AA forcing response drives a -0.11 mm day^{-1} drying for the 1970s − 1950s and a 0.17 mm day^{-1} wetting for the 2000s − 1970s, which are 85% and 96% of the ALL-forcing response in their respective periods.

Calculating the minimum precipitation year in the 11-yr rolling averaged JAS precipitation time series for individual ALL ensemble members between 1950 and 2020, we find the average year of peak drying conditions among members of the ALL forcing LEs is 1977 for both CESM1 and CanESM2 with standard deviations of 12 and 10 years, respectively. Thus, the observed peak drought timing of ~1986 (with some spread among the observational datasets) is consistent with the internal variability of the LEs. However, a comparison to the observed precipitation records shows that both CESM1 and CanESM2 substantially underestimate the magnitude of the multidecadal variability (black curves in Fig. 3), as the precipitation anomalies for all four observation datasets fall outside the range given by the ensembles. The inability of the CESM1 LE to capture this multidecadal variability is also shown by McKinnon and Deser (2018), who found that the CESM1 LE underestimates the variability of 50-yr JJA precipitation trends throughout sub-Saharan Africa relative to an observational LE derived estimate of internal variability. This is a deficiency that is common among CMIP5 models (Biasutti 2013; Undorf et al. 2018), although some coupled models are able to produce larger precipitation trends (Held et al. 2005; Ackerley et al. 2011).

Analyses of AMIP simulations which are forced by historical observed SSTs and sea ice have found that some models are able to capture multidecadal variability of a similar magnitude to observations (Giannini et al. 2003; Lu and Delworth 2005; Held et al. 2005; Caminade and Terray 2010; Hoerling et al. 2006). However, the ability to reproduce the observed response varies among AGCMs. For example, an analysis of multiple AGCMs by Scaife et al. (2009) found that only one of the models they analyzed could reproduce the magnitude of the more severe 1950–80 drying trend. We are able to update some of this analysis with simulations carried out for the AGCMs we studied here. Comparing the Sahel precipitation time series for CAM5 C20C+ (Fig. S3a) and CanAM4 AMIP (Fig. S3b) simulations to the ALL LE simulations, we find that, compared to the LE, CAM5 C20C+ sees larger multidecadal variability that better matches the observed variability while CanAM4 AMIP sees relatively little change in its decadal variability. Thus, it appears that CESM1 underestimates the observed variability in large part because it does not capture historical coupled ocean–atmosphere SST variability, while for CanESM2 there is a lack of sensitivity of Sahel precipitation to SST anomalies even in the absence of possible errors in SST variability.

As mentioned in section 2, for CESM1 we can partially check the additivity assumption that the responses to AER are equivalent to the ALL responses minus the XAER responses. Figure 3a shows the three-member AER ensemble along with the ALL minus XAER ensemble. The two protocols have similar Sahel precipitation trajectories, suggesting that there is reasonable additivity between the response to AA forcing and other external forcings such as GHG for this variable and region. In addition, we find that the regional drying does not appear to be amplified in the ALL simulations (where GHG and AA are both present) relative to the AER simulations in CESM1 and CanESM2. Thus, these models do not show direct evidence for enhanced drying in response to combined GHG and AA forcing as proposed by Giannini and Kaplan (2019).

Figure 4 displays the JAS mean sulfate (SO_4) burden anomalies from the CESM1 and CanESM2 LEs. The 1970s − 1950s

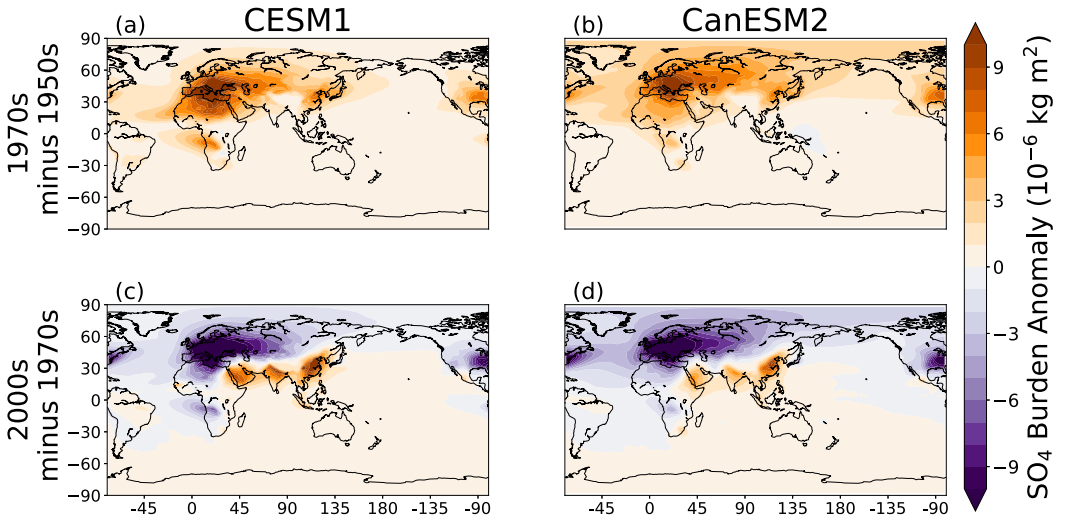

FIG. 4. JAS mean sulfate burden anomalies for the (top) 1970s − 1950s and (bottom) 2000s − 1970s from (a),(c) CESM1 ALL–XAER LE and (b),(d) CanESM2 AER LE.

period is characterized by widespread increases in sulfate, especially in the North Hemisphere near and downwind of European and North American industrial regions (Figs. 4a,b). There is a local increase of sulfate over the Sahel during this period due in part to emissions being transported from Europe. The sulfate anomalies are transported farther in CanESM2, resulting in greater anomalies in the North Atlantic, North Pacific, and Arctic relative to CESM1. For the 2000s − 1970s, there are decreases in sulfate burdens in much of the North Hemisphere extratropics associated with declining North American and European emissions. Continued increases occur in East Asia, South Asia, and the Middle East. Locally, there is a decline in concentrations over the Sahel which is likely due to decreasing transport from Europe, offset by increasing local emissions and transport from the Middle East.

Black carbon (BC) burdens increase locally over the Sahel in both periods (Fig. S4), with much larger increases in CanESM2 because of the inclusion of BMB emissions. BC burdens increase over Asia in both periods and decrease over eastern North America and western Europe in both periods. The effect of BMB emissions is evaluated using the CESM1 LE XBMB simulations. BMB changes result in large BC burden increases over central Africa in the drying period (Fig. S5b). However, unlike CanESM2, there is no decline in BC burdens in the recovery period (Fig. S5d), indicating there is some discrepancy in emissions between the models. In addition, we see increasing sulfate burdens from central Africa in the drying period (Fig. S5a) and declining burdens over the Europe and Northern Africa in the recovery period (Fig. S5c), although these BMB anomalies are an order of magnitude smaller than the anomalies due to industrial emissions in Fig. 4. BMB aerosol changes result in increased precipitation in the Guinea region in both periods (Figs. S6a,c), with a small contribution to the aerosol-forced drying and recovery of Sahel precipitation. Thus, industrial AA emissions are the main drivers of AA-forced Sahel precipitation change in CESM1, with BMB emissions playing a minor role in amplifying the overall aerosol-forced signal in the Sahel.

Figure 5 displays the JAS mean AA-forced SST and SIC responses from the LEs in the drying and recovery periods. These are representative of the boundary conditions used to force the AGCM simulations described in section 2b (Table 2; see also Table S1). Both CESM1 and CanESM2 have broadly similar SST anomalies, although CESM1 sees larger anomalies due in part to the larger aerosol ERF in the model (Zelinka et al. 2014). In the drying period, there is widespread cooling that is strongest in the Northern Hemisphere. In the recovery period, the SST anomalies change sign in the North Hemisphere, with both models showing warming in the North Atlantic and the midlatitude and subpolar North Pacific. However, there is continued cooling in the Indian Ocean and tropical west Pacific, downwind of Asian regions that undergo continued AA emission increases. Arctic SIC responses follow the Northern Hemisphere SST response, with an increase in Arctic SIC in the drying period and a decline in the recovery period. In CESM1 we see an increase in SIC in parts of the Arctic during the recovery period. This appears to be an artifact of subtracting anomalies from the ALL and XAER simulations, which both lose sea ice but do so in different regions due to their differing sea ice covers. Changes to Antarctic SIC and Southern Ocean SST are small as AA forcing is weak in this region.

The AA-forced multidecadal SST change in the North Atlantic in the LEs (Fig. 5) results in a reversal of the hemispheric asymmetry of SST anomalies between the two periods. Based on previous arguments (e.g., Ackerley et al. 2011), this reversal of the hemispheric asymmetry of SST anomalies both in the Atlantic and globally would appear to be responsible for the reversal of AA-forced Sahel precipitation anomalies. However, past studies in coupled models could not explicitly establish a causal link between the hemispheric asymmetry and Sahel precipitation as this ocean-mediated effect was not

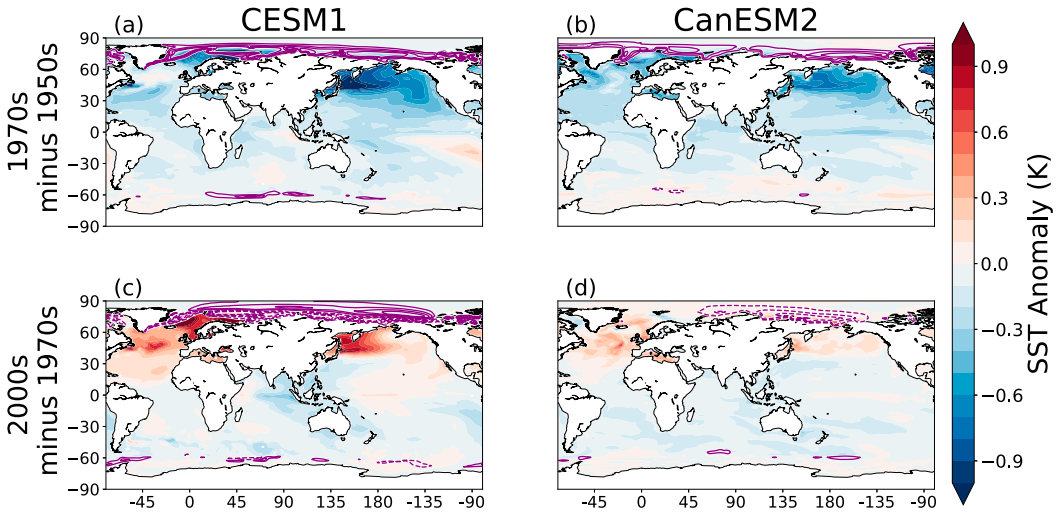

FIG. 5. As in Fig. 4, but for the AA-forced SST anomalies. Sea ice concentration anomalies are displayed in purple contours in 2.5% intervals.

isolated from the direct-atmospheric effect. Thus, we seek to better understand the mechanisms underlying the coupled GCM responses by conducting AGCM experiments to separate the influence of SSTs from the influence of the aerosols themselves. Indeed, a key takeaway from the AGCM experiments discussed below is that the direct-atmospheric response to AA forcing plays a substantial and at times competing role with the ocean-mediated response. In particular, it is the direct-atmospheric response rather than the ocean-mediated response that mainly drives the 1970s − 1950s drying in CAM5 and CanAM4.

4. Direct-atmospheric and ocean-mediated responses

a. Evaluation of AGCM simulations

We hypothesize that the total AA response (direct-atmospheric plus ocean-mediated response) in our prescribed SST/sea ice AGCM simulations is close to the coupled response to AA forcing from the LE simulations as the atmosphere in both cases experience approximately the same perturbations. To evaluate the ability of the AGCM simulations to reproduce the coupled LE response in light of potential errors due to the AGCM protocol and fixed-SST conditions, the two sets of simulations are compared for the 1970s − 1950s in Fig. 6 and the 2000s − 1970s in Fig. S7. We find that for the 1970s – 1950s the CAM5 simulations (Fig. 6c) can reasonably reproduce the JAS African precipitation response from the CESM1 LE (Fig. 6a), while the CanAM4 (Fig. 6d) simulations only capture part of the drying seen in the CanESM2 LE (Fig. 6b). The spatial correlation between the LE and AGCM simulations over global land (African land) is 0.43 (0.42) for CAM5 and 0.35 (0.14) for CanAM4. The agreement between the LE and AGCM improves for the 2000s − 1970s (Fig. S7), with spatial correlations for global land (African land) being 0.68 (0.68) for CAM5 and 0.51 (0.63) for CanAM4. This may be because the 1970s − 1950s response is noisier as it is calculated as the difference of two experiments. Although there are discrepancies in the pattern of response, the regionally averaged Sahel precipitation anomalies in the AGCM simulations are consistent with those in the coupled LE simulations, as we discuss below (section 4d; Fig. 12).

Thus, while there are errors arising from the idealized nature of the AGCM simulations, the CAM5 simulations can capture the broad characteristics of the response. However, the CanAM4 simulations can only do so in the recovery period. Furthermore, CanAM4 is unable to reproduce historical Sahel precipitation variability given observed SST change, suggesting Sahel climate in this model is insufficiently sensitive to SST forcing (Fig. S3b). Thus, the subsequent discussion first centers on the CAM5 AGCM simulations, which provide the clearest signals that are most consistent with the coupled model response. We then return to the CanAM4 simulations, which provide intriguing points of comparison with CAM5.

b. CAM5 results

The CAM5 experiments reveal that distinct mechanisms drive the precipitation changes during the drying and recovery periods in the Sahel (Fig. 7). For the 1970s − 1950s, the drying seen across much of NH Africa in the total response is dominated by the direct-atmospheric response (Fig. 7b), with a weak ocean-mediated wetting over the Sahel (Fig. 7c). This pattern of direct-atmospheric drying is consistent with other studies of the direct-atmospheric response to sulfate aerosol forcing (Dong et al. 2014; Richardson et al. 2016). However, the dominance of the direct-atmospheric response contrasts with the view that AA-forced Sahel drying is a primarily ocean-mediated response caused by a southward shift of the ITCZ in response to hemispherically asymmetric SST anomalies (e.g., Biasutti and Giannini 2006; Ackerley et al. 2011; Hua et al. 2019). One potential explanation for the lack of ocean-mediated precipitation response in this period may be cancelling effects from SST anomalies in different basins. In CESM1

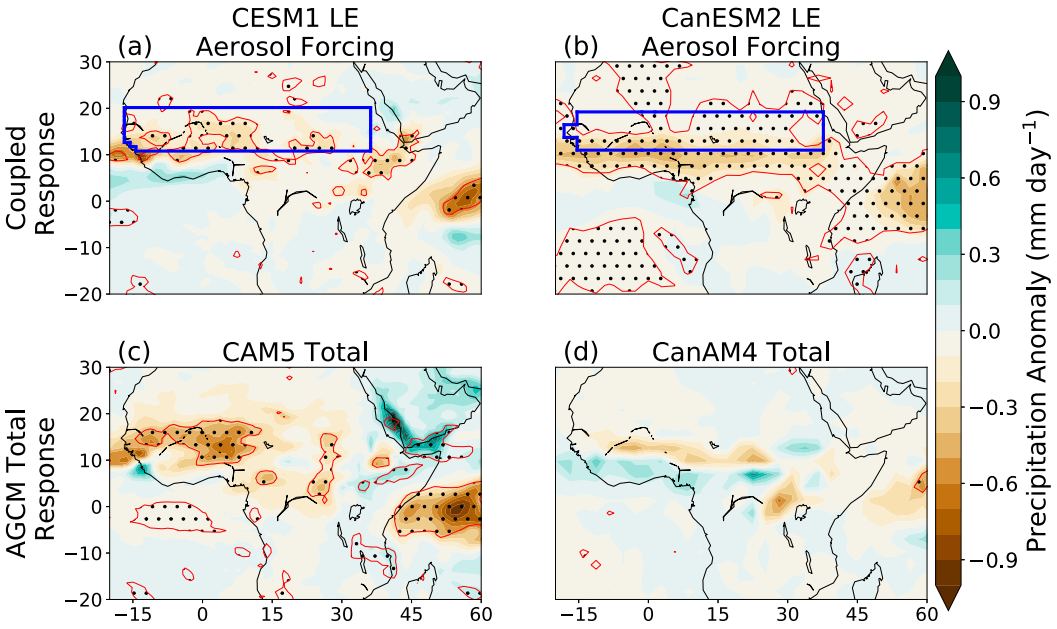

FIG. 6. Comparison of the AA-forced 1970s − 1950s JAS precipitation anomalies for the coupled LE (a) CESM1 and (b) CanESM2 compared to the total (direct-atmospheric + ocean-mediated) response in their respective atmosphere models: (c) CAM5 and (d) CanAM4. Note that (a) and (b) are the same as Figs. 1b and 2b, respectively. Stippling and thin red contour indicates responses that are significant at the 95% level using a point-wise *t* test. The blue boxes indicate the averaging region used in Fig. 12.

for this period (Fig. 5a), the aerosol radiative cooling gives rise to patterned cooling of comparable strength in the North Atlantic, the tropical Atlantic and Pacific, and the Indian Ocean. Previous literature suggests that such regional responses could cause interfering responses in the Sahel: cool North Atlantic and Mediterranean SSTs are associated with drying in the Sahel while cool Indian Ocean, cool tropical Atlantic, and warm east tropical Pacific SSTs are associated with wetting in the Sahel (Giannini et al. 2008; Mohino et al. 2011; Dyer et al. 2017).

A simplified picture of this cancellation can be evaluated using the North Atlantic Relative Index (NARI), which is defined as the spatial average of SSTs in the subtropical North Atlantic (10°–40°N, 75°–15°W) minus tropical ocean (20°S–20°N)

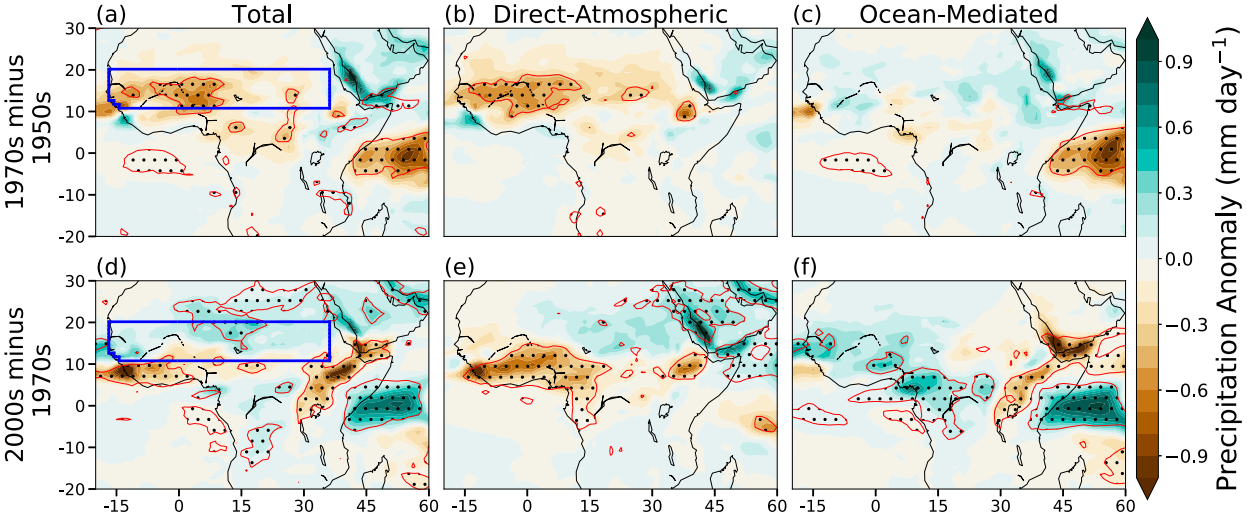

FIG. 7. (left) Total, (center) direct-atmospheric, and (right) ocean-mediated components of the JAS precipitation response to AA forcing in CAM5 for the (a)–(c) 1970s − 1950s and (d)–(f) 2000s − 1970s. The stippling and the thin red contours indicate responses that are significant at the 95% level using a point-wise *t* test. The blue boxes indicate the averaging region used in Fig. 12.

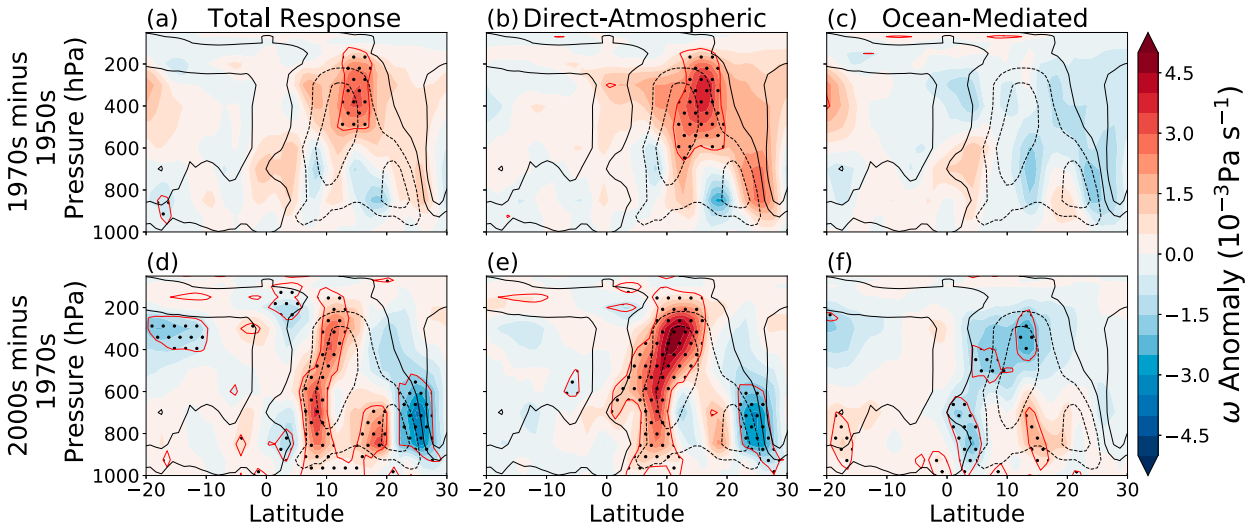

FIG. 8. As in Fig. 7, but for JAS vertical velocity ω zonally averaged over Africa (15°W–35°E). Black contours indicate the climatological vertical velocity in intervals of 0.1 Pa s^{-1}.

(Giannini et al. 2013). This index is positively correlated with Sahel precipitation in both observations and coupled model simulations (Giannini et al. 2013; Giannini and Kaplan 2019). The CESM1 AER LE SSTs have a NARI anomaly of −0.09 K for the 1970s and 1950s, which would be expected to cause ocean-mediated drying in the Sahel. The weak wetting thus indicates that the remaining contributions from the patterned SST response have an additional wetting effect on the Sahel that is not accounted for. Nevertheless, the NARI change suggests that the AA-forced response mediated through North Atlantic cooling (−0.23°C) may be partially countered by the cooling in the global tropical oceans (−0.14°C).

For the 2000s − 1970s, the CAM5 ocean-mediated response (Fig. 7f) causes increased precipitation across much of Africa, particularly in the western Sahel and Congo basin, with direct-atmospheric drying on the Guinea Coast and weak wetting over the eastern Sahel (Fig. 7e). Thus, the increasing Sahel precipitation appears to be mostly an ocean-mediated response, with an additional contribution or cancellation from the direct-atmospheric response depending on the region. In this period, the SST anomalies across the basins tend to be those that are associated with increased precipitation in the Sahel, with warmer North Atlantic SST and cooler Indian Ocean, tropical Atlantic, and east tropical Pacific SST (Fig. 5c). These anomalies result in a positive NARI anomaly of 0.18 K for the 2000s − 1970s, which aligns with the ocean-mediated response we see in the AGCM results. The direct-atmospheric drying response of the coastal West Africa occurs in spite of relatively small changes in sulfate burden in the region and large declines in AA emissions from North America and Europe and may be a remote impact of increasing AA emissions from Asia, similar to that reported by Dong et al. (2014). Thus, what appears in the total response to be a northward shift of precipitation over Africa extending from the shift in the tropical Atlantic ITCZ (Figs. 1c and 7d) actually results from a combination of opposing but spatially offset direct-atmospheric and ocean-mediated responses.

The CAM5 direct-atmospheric and ocean-mediated responses of zonally averaged vertical velocity over Africa align with the precipitation responses in the model (Fig. 8). The direct-atmospheric response causes a weakening of tropical upwelling for both periods (Figs. 8b,e). In the recovery period, the downwelling anomaly shifts south, resulting in weak zonally averaged changes in the Sahel north of 15°N and upwelling in the Sahara north of 20°N. This change in the response aligns with the southward shift of the drying anomaly and weak wetting in the northern Sahel and Sahara. The ocean-mediated response causes weak upwelling anomalies over the Sahel during the drying period (Fig. 8c). In the recovery period, the upwelling anomalies strengthen above the Sahel (Fig. 8f). These responses are consistent with competing and latitudinally separated direct-atmospheric and ocean-mediated precipitation responses remarked on above. Thus, the changing total response over the Sahel between the two periods is the result of the strengthening of the ocean-mediated upwelling combined with the weakening of the direct-atmospheric downwelling north of 15°N.

That the direct-atmospheric response drives subsidence for the drying period hearkens back to the model of Charney (1975) in which subsidence occurs as a response increasing net albedo in desert regions. Although this was originally discussed in the context of surface albedo change, one could also interpret this change in net albedo as a change in shortwave forcing by aerosols over the Sahara and Sahel. On the other hand, there is continued direct-atmospheric drying for the recovery period extending from coastal regions of West Africa into the western Sahel in spite of the relatively small local changes in sulfate burden. Thus, a view of the direct-atmospheric response as wholly driven by local perturbations to shortwave radiation in the Sahel is incomplete, as there can be dynamically

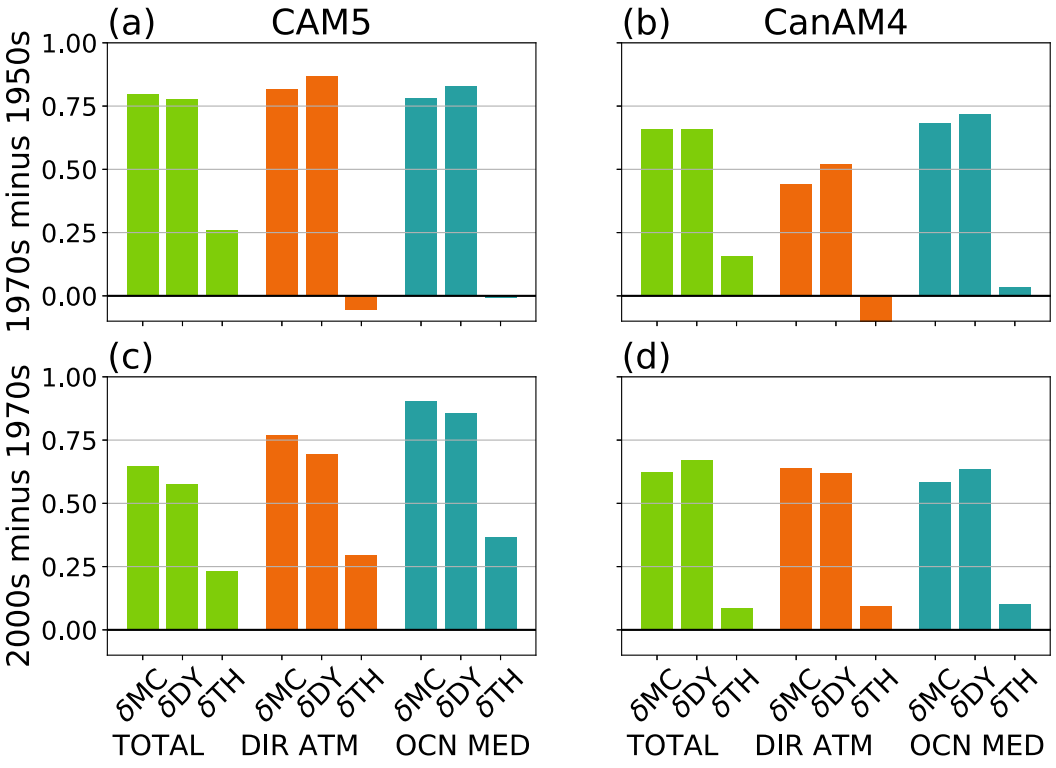

FIG. 9. Correlation coefficient between the $P - E$ anomaly field to the mean flow total (δMC), dynamic (δDY), and thermodynamic (δTH) moisture convergence anomalies over NH Africa (0°–20°N, 20°W–35°E) for the (top) 1970s − 1950s and (bottom) 2000s − 1970s in (a),(c) CAM5 and (b),(d) CanAM4. For each case, the total (TOT; green), direct-atmospheric (DIR ATM; orange), and ocean-mediated (OCN MED; blue) response bar plots are shown with the total (δMC), dynamic (δDY), and thermodynamic (δTH) mean flow moisture convergence from left to right.

driven drying due to teleconnected circulation responses to remote emissions (Dong et al. 2014).

Further analysis of the AGCM response is conducted using moisture convergence analysis to decompose the $P - E$ change into mean flow dynamic (δDY) and thermodynamic (δTH) components (section 2c). Over the Guinea Coast and Sahel region south of 15°N, the total mean flow component explains most of the change in $P - E$, while the eddy component plays a more pronounced role north of 15°N (Fig. S8 for CAM5; Fig. S9 for CanAM4). To determine the relative roles of the dynamic and thermodynamic moisture convergence, we calculate the spatial correlation coefficient between $P - E$ and the mean flow moisture convergence components over NH Africa (0°–20°N, 15°W–35°E) (red boxes in Figs. S10 and S11). We find that for CAM5 (Figs. 9a,c), δDY explains most of the $P - E$ change for the total, direct-atmospheric, and ocean-mediated responses in both periods, with δTH accounting for a relatively small portion of the change. These results suggest that AA-forced precipitation changes over continental Africa are largely dominated by changes to circulation in the region, which aligns with similar analysis performed for changes to Asian monsoon circulation (Li et al. 2018). This is expected in the case of the direct-atmospheric response as the fixed SSTs cause little change in moisture supply. On the other hand, the small thermodynamic component of the ocean-mediated response indicates that increasing moisture supply from warming SSTs in the North Atlantic and Mediterranean during the recovery period play a relatively minor role in driving the precipitation increase.

c. *CanAM4 results*

Although the precipitation response in CanAM4 is noisier and weaker than in CAM5 (Fig. 10), aspects of direct-atmospheric and ocean-mediated responses appear to be qualitatively similar. The generally weak signals reflect CanAM4's smaller sensitivity to SST anomalies as demonstrated by its response to observed SST changes (Fig. S3b) as well as weaker AA ERF and local feedbacks, such as smaller changes in the interactive dust emissions in CanAM4 (not shown), which act as a positive feedback on Sahel precipitation anomalies (e.g., Pausata et al. 2016). For the 1970s − 1950s, there is drying in the Sahel (Fig. 10a) that is caused by a direct-atmospheric drying (Fig. 10b), which is partially canceled by ocean-mediated wetting (Fig. 10c). For the 2000s − 1970s, there is an increase in precipitation over the Sahel in the total response (Fig. 10d) that is dominated by the ocean-mediated response (Fig. 10f), but also has a contribution from a direct-atmospheric wetting response (Fig. 10e).

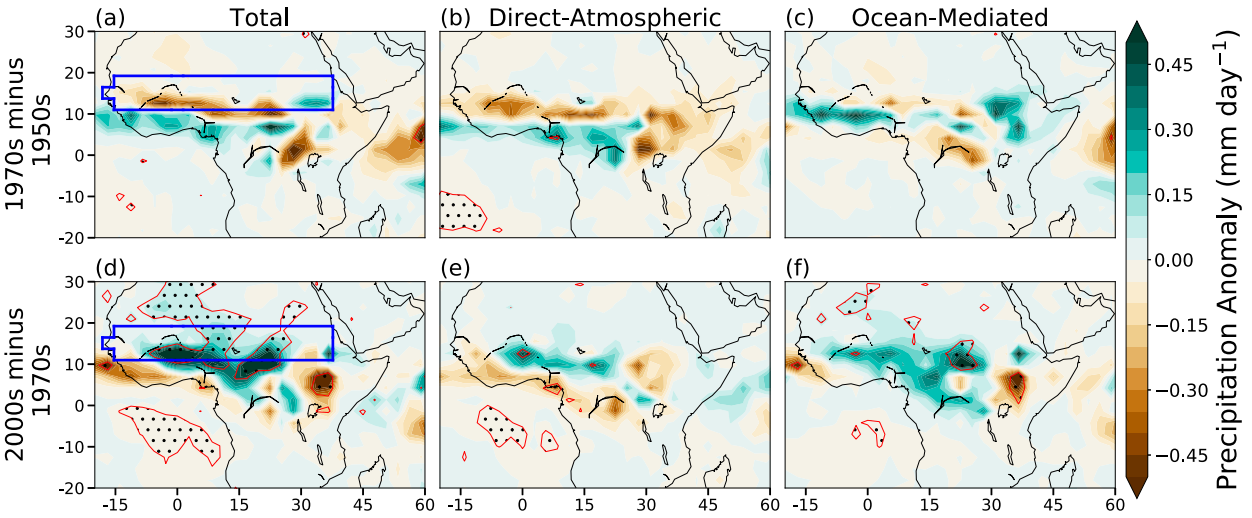

FIG. 10. As in Fig. 7, but for CanAM4 precipitation. Note that the color scale is halved relative to the CAM5 response in Fig. 7.

The moderate drying period ocean-mediated wetting in these runs is contrary to our expectations from the −0.08-K NARI anomaly in the CanESM2 AER LE, which we expect to correspond to Sahel drying, although again we see cancellation between North Atlantic (−0.25°C) and global tropical (−0.17°C) SST anomalies. On the other hand, the +0.08-K anomaly for the recovery period aligns with the ocean-mediated wetting in the AGCM results. CanAM4 resembles CAM5 in that drying seen for the drying period is driven by the direct-atmospheric response, and the wetting seen for the recovery period is driven by the ocean-mediated response. However, the models differ in that CanAM4 sees a larger relative contribution from direct-atmospheric wetting in the recovery period.

In the drying period CanAM4, like CAM5, shows a direct-atmospheric downwelling response (Fig. 11b) and an ocean-mediated upwelling response (Fig. 11c) in the ITCZ. In the recovery period, the direct-atmospheric vertical velocity response is diminished and reverses sign (Fig. 11e) while there continues to be an ocean-mediated upwelling response (Fig. 11f). Thus, the models have qualitative agreement on the sign of the circulation response to the AA-forced direct-atmospheric and ocean-mediated responses, except in the case of the recovery period direct-atmospheric response.

Analysis of the $P - E$ response using moisture convergence shows that, as in CAM5, the dynamic component dominates over the thermodynamic component (Figs. 9b,d). However, we see that the total mean flow moisture convergence has a lower correlation with the $P - E$ for some of the responses, with correlation coefficient of less than 0.5 for the direct-atmospheric response for the 1970s − 1950s. Again, this may be due to the noisy nature of the precipitation response as the

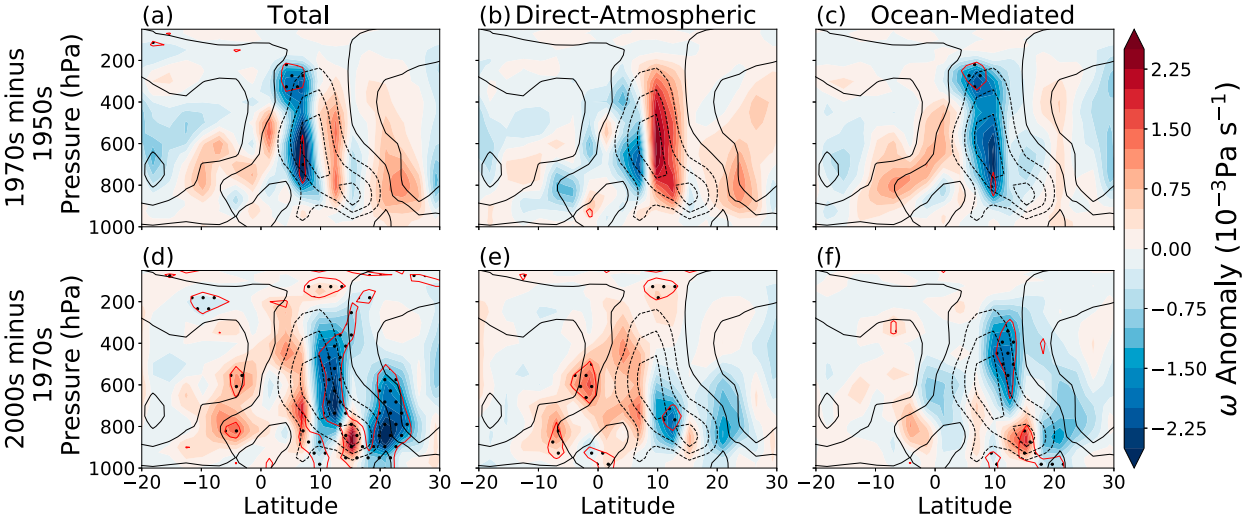

FIG. 11. As in Fig. 8, but for the CanAM4 response. Note that the color scale is halved relative to the CAM5 response in Fig. 8.

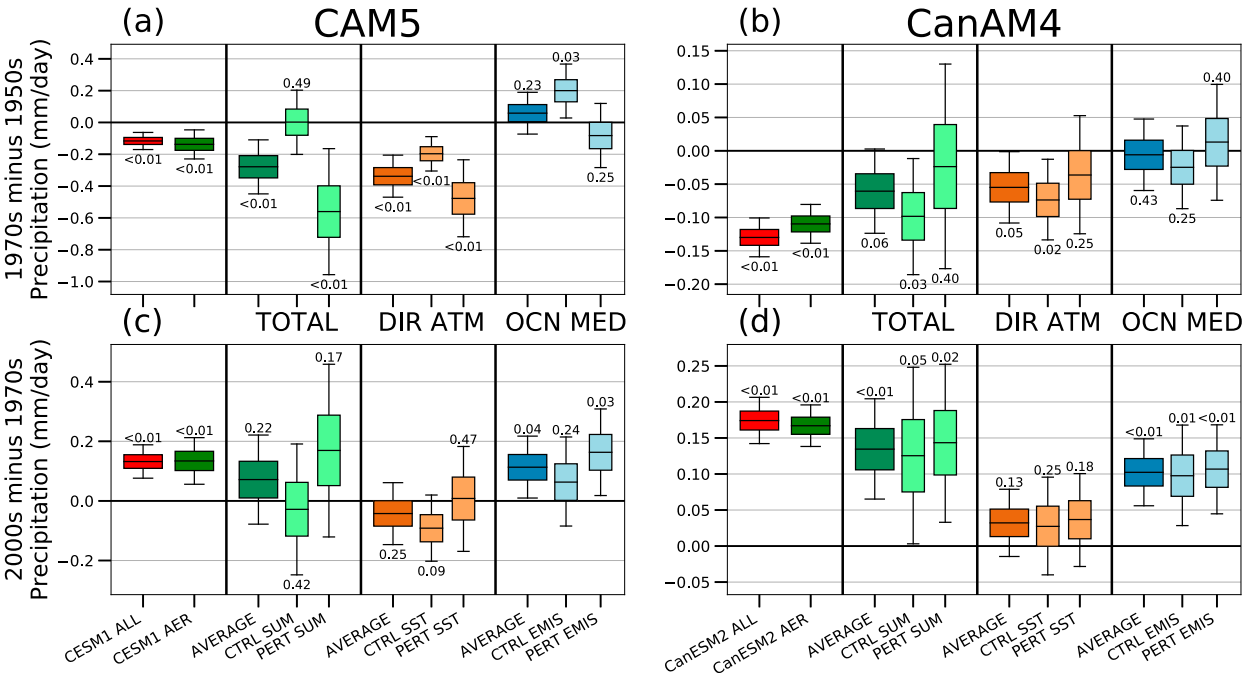

FIG. 12. Boxplots showing the distribution of means obtained via bootstrap resampling ($n = 10^5$) of regionally averaged Sahel (10°–20°N and 20°W–35°E, excluding ocean grid points) precipitation change in the (a),(c) CAM5 and (b),(d) CanAM4 simulations for the (top) 1970s − 1950s and (bottom) 2000s − 1970s. The boxes display the interquartile range and the whiskers display the 5th–95th percentile range of bootstrapped means. The fraction of bootstrapped means above or below 0 (i.e., the p value) is displayed next to the whiskers of each box. The coupled LE response to all and AA forcing is shown on the far left of each panel in red and green, respectively. These are followed by the total, direct-atmospheric (DIR ATM), and ocean-mediated (OCN MED) responses in green, orange, and blue from left to right. The darker shaded boxes show the differences shown in Figs. 7–11 and are the means of their two respective lighter shaded boxes. Lighter shaded boxes display the two methods for calculating each of the responses using different combinations of AGCM simulations as described in Table S1 and are used to assess nonlinearity in the responses.

correlation tends to be lower for the experiments with weaker responses.

d. Analysis of regional mean precipitation anomalies

To synthesize the experiments considered here we assess the regionally averaged Sahel precipitation anomalies in Fig. 12. This figure displays the distribution of epoch differences (1970s − 1950s and 2000s − 1970s) of regional mean Sahel precipitation in the LE and AGCM simulations obtained via bootstrap resampling of the years in the simulations, with the whiskers showing the 5th–95th percentile ranges of the bootstrapped means. As we assume each year is independent of the others in the bootstrap resampling, this likely underestimates the spread in the sample means. The information in Fig. 12 is arranged as follows, from left to right: ALL (red) and AER (green) responses from the coupled LE simulations; total (green) responses from the AGCM experiments; direct-atmospheric (orange) responses from the AGCM experiments; and ocean-mediated (blue) responses from the AGCM experiments. Each of the AGCM responses is computed using two different methods (see Table S1; lighter boxes) as well as the average of the two methods (darker boxes). By comparing the bootstrap distributions for the different methods for calculating each response, we can then assess potential nonlinearities found in the direct-atmospheric and ocean-mediated responses.

We find that the 5th–95th percentile ranges (whiskers in Fig. 12) of all-forcing and AA-forcing LE responses overlap for CESM1 and CanESM5, for both periods, consistent with Fig. 3. Furthermore, the AGCM 5th–95th percentile ranges of the total responses encompass the mean coupled LE AA-forced responses for both periods and both models. Thus, the AGCMs appear to be consistent with the corresponding LEs in the regional average. The range of the bootstrapped mean total AGCM anomalies suggests that internal variability is partially responsible for the discrepancy in the anomaly patterns in the AGCMs versus the LEs.

In CAM5, the 1970s − 1950s direct atmospheric and total drying signals are statistically significant while the weak ocean-mediated wetting is not (Fig. 12a). However, there are notable nonlinearities in the responses. We evaluate the nonlinearity by comparing the sum of the CTRL SST direct-atmospheric and CTRL EMIS ocean-mediated responses (labeled as the "CTRL SUM" response in the "TOTAL" column in Fig. 12) to the response when the two components are applied simultaneously (AVERAGE TOTAL response) (Fig. S10). For this period, the CTRL SUM total response has a weaker drying throughout the Sahel relative to the AVERAGE total response

(Fig. S10c). As a result, the regional average CTRL SUM total response is near zero and falls outside the 5th–95th percentile range of the AVERAGE total response. Thus, there are nonlinear interactions between the direct-atmospheric and ocean-mediated responses that result in statistically significant ($p = 0.028$) differences between the regionally averaged AVERAGE and CTRL SUM total responses (Fig. 12a). This is due to weaker CTRL SST direct-atmospheric (''DIR ATM'' column) drying compared to PERT SST and stronger, statistically significant CTRL EMIS ocean-mediated (''OCN MED'' column) wetting compared to the weak drying seen in the PERT EMIS case. Thus, while the nonlinearity significantly affects the magnitude of the responses, the interpretation of the relative roles of the responses remains the same, with the direct-atmospheric response driving drying in either case.

In the 2000s − 1970s, the CAM5 ocean-mediated wetting is significant while the direct-atmospheric and total responses are not significant (Fig. 12c) due to opposite signed responses in the northern versus southern Sahel (Figs. 7d,e). Comparing the CTRL SUM and AVERAGE total response we find the latter has more recovery period wetting in the eastern Sahel (Figs. S10d–f), that passes our statistical significance criterion in some grid boxes. However, the nonlinearity is not significant in the regional average for this period (Fig. 12c; $p = 0.18$), although we see that using different combinations of experiments can yield differing statistical inferences, with the AVERAGE and PERT EMIS ocean-mediated responses having significant wetting signals while the CTRL EMIS response is not significant.

In CanAM4 for the Sahel averaged, there is a significant 1970s − 1950s direct-atmospheric drying, a near-zero ocean-mediated response, and a total drying response that is marginally not significant (Fig. 12b). In the 2000s − 1970s, there is an ocean-mediated wetting that is significant and a weaker direct-atmospheric wetting response that is not, which combined show a significant total wetting signal (Fig. 12d). There is little statistically significant nonlinearity in CanAM4 for either period (Figs. S11c,f), although the magnitude of the nonlinearity is larger for the drying period than the recovery period, again as the former is the residual of two experiments and is thus noisier than the latter. The nonlinearities are not significant (Figs. 12b,d) in the Sahel regional average. However, as in CAM5, certain statistical inferences differ depending on the method of calculating the response. Namely, the drying period CTRL SUM total and CTRL SST direct-atmospheric responses are significant though their average changes are not.

5. Conclusions

By using the single forcing simulations from the CESM1 and CanESM2 LEs to isolate externally forced Sahel precipitation variability from internal variability, we find that it is AA forcing rather than GHG forcing that dominates the externally forced component of both the Sahel drought and recovery in the late twentieth century in both models. However, while the forced precipitation variability in the LEs has similar timing to that of the observed Sahel precipitation variability, the LEs substantially underestimate the magnitude of the variability. Thus, it is difficult to determine the relative roles of external forcing and internal variability in these models. Nonetheless, the single forcing LE simulations prove particularly important for deciphering the influence of AA forcing on regional climate, due to the spatially nonuniform and temporally nonmonotonic changes in aerosol and precursor emissions. As a result, AA forcing can have impacts on multidecadal time scales that might be difficult to robustly identify with smaller ensembles.

Using AGCM experiments designed to capture multidecadal AA-forced changes in the coupled GCMs, we find that the direct-atmospheric and ocean-mediated responses have distinct, and at times competing, roles in driving multidecadal AA-forced Sahel climate variability. The CAM5 AGCM simulations are able to reproduce the coupled LE response, while the CanAM4 AGCM simulations can only do so for the recovery period. In the drying period (1970s − 1950s), AA-forced Sahel drying is largely caused by the direct-atmospheric response with a weak ocean-mediated wetting response. This apparently contrasts with the hypothesis that AA-forced Sahel precipitation variability is predominantly a response to hemispheric asymmetries in SST anomalies (Held et al. 2005; Ackerley et al. 2011; Mohino et al. 2011; Wang 2015). Although we cannot determine why the CAM5 ocean-mediated component of the response is so weak, we hypothesize that it may be a result of competing influences from different ocean basins. If this is indeed the case, this aspect of the response is likely to be sensitive to model differences in the pattern and strength of AA forcing and the corresponding SST response. In the recovery period (2000s − 1970s), the ocean-mediated response is the main driver of the increase in Sahel precipitation with the direct-atmospheric response causing drying in the southern Sahel and wetting in the northern Sahel in CAM5 and having moderate wetting effect in CanAM4. The two models have qualitatively more consistent direct-atmospheric and ocean-mediated vertical velocity responses in the two periods, but CAM5 has stronger and more coherent responses.

The AGCM protocol used here has notable limitations including possible errors arising from the lack of atmosphere–ocean coupling and the fact that the 1970s − 1950s responses are calculated as the residual of two sets of experiments and thus are noisier and likely less robust than the 2000s − 1970s. Furthermore, when separating the ocean-mediated and direct-atmospheric effects we find that there are nonlinear effects indicating that forced Sahel precipitation response is sensitive to background SST and emission conditions. The differences between the responses in the experiments described here hints at wider intermodel uncertainty regarding the relative roles of direct-atmospheric and ocean-mediated responses in determining the regional climate response to anthropogenic aerosol forcing. As these effects can compete, their model dependence compounds uncertainty in the Sahel precipitation response to aerosols, mirroring the uncertainty resulting from the opposing responses to direct-atmospheric GHG forcing versus SST warming (Biasutti 2013; Gaetani et al. 2017). Furthermore, the differing multidecadal variability of CAM5 and CanAM4 in AMIP-style experiments indicates that there are substantially different sensitivities to SST variability between the models. Such analysis reinforces the utility of longer-term AMIP-style

simulations as an avenue for understanding coupled GCM errors in comparison to observations, such as those produced for the C20C+ project (e.g., Stone et al. 2018). Nevertheless, the qualitative agreement between the models in spite of these differences suggests the relative roles of the direct-atmospheric and ocean-mediated effects over the two periods examined here may be relatively robust.

The experiments described here suggest that the AA-forced response of Sahel precipitation cannot be solely understood in terms of SST anomalies feeding back on the atmosphere. Instead, the direct-atmospheric response to the forcing also plays a key role in the forced response. Due to the potential role of the direct-atmospheric response to AA forcing, correlations between multidecadal SST variability and Sahel precipitation derived from observations and coupled ocean–atmosphere GCM simulations may not necessarily imply a direct causal link. Rather, they may covary in part due to common influence from external forcing.

Because AA and precursor emissions are expected to decline into the future (Gidden et al. 2019), we expect further AA-forced increases in Sahel precipitation. Indeed, analysis of the CESM1 XAER large ensemble suggests that AAs will continue to have a major contribution to Sahel precipitation increases up to the mid-twenty-first century (not shown). However, the ALL and AER simulations in CanESM2 begin to diverge in the 2000s (Fig. 3b), indicating that GHG dominate future changes in that model. Thus, it appears that the CAM5 and CanAM4 disagree regarding the magnitude of the AA effect on the Sahel into the future. The direct-atmospheric response to AA will likely contribute to the continued recovery of Sahel precipitation as emissions from Asia and Africa begin to decline. As long as emission reductions in Asia lag behind reductions in Europe and North America, there will be future AA-forced SST warming that is strongest in the North Atlantic and Pacific with weaker warming in the Indian and tropical Pacific, resulting in an increase in the NARI. Thus, we might expect further near-term ocean-mediated wetting of the Sahel in response to AA forcing.

The contrasting roles of direct-atmospheric and ocean-mediated responses for the drying and recovery periods emphasizes the importance of considering the transient response when studying the influence of AA on regional climate. Assessing the full preindustrial to present-day response can give an incomplete picture of the effect of AA on Sahel precipitation by obscuring aspects of the transient response such as the timing of direct-atmospheric and ocean-mediated influences on regional climate. Analysis of transient AGCM simulations from CMIP6 endorsed MIPs such as AerChemMIP (Collins et al. 2017) will provide an opportunity to gain further insight into the role of direct-atmospheric and ocean-mediated responses in driving the regional climate response to AA forcing.

Acknowledgments. We thank Thomas Oudar for his helpful input to the study, the staff at SciNet for their assistance in completing our simulations, and the *Journal of Climate* reviewers and editor for their valuable discussion on the manuscript. This work was supported by funding from Environment and Climate Change Canada and the National Science and Engineering Research Council of Canada. Computations were performed on the Niagara supercomputer at the SciNet HPC Consortium. SciNet is funded by the Canada Foundation for Innovation; the Government of Ontario; Ontario Research Fund–Research Excellence; and the University of Toronto. This material is based in part on work supported by the National Center for Atmospheric Research, which is a major facility sponsored by the National Science Foundation (NSF) under Cooperative Agreement 1852977. CESM1 LE data are available from ESG at http://www.cesm.ucar.edu/projects/community-projects/LENS/data-sets.html?ref=hp. The CESM project is supported primarily by the NSF. CanESM2 LE data are available from the Environment Canada and Climate Change Canada at https://open.canada.ca/data/en/dataset/aa7b6823-fd1e-49ff-a6fb-68076a4a477c. U. Delaware, PREC/L, and GPCC precipitation data provided by the NOAA/OAR/ESRL PSD, Boulder, Colorado, USA, from their Web site at https://www.esrl.noaa.gov/psd/.

REFERENCES

Ackerley, D., B. B. B. Booth, S. H. E. Knight, E. J. Highwood, D. J. Frame, M. R. Allen, and D. P. Rowell, 2011: Sensitivity of twentieth-century Sahel rainfall to sulfate aerosol and CO_2 forcing. *J. Climate*, **24**, 4999–5014, https://doi.org/10.1175/JCLI-D-11-00019.1.

Andrews, T., P. M. Forster, and J. M. Gregory, 2009: A surface energy perspective on climate change. *J. Climate*, **22**, 2557–2570, https://doi.org/10.1175/2008JCLI2759.1.

Biasutti, M., 2013: Forced Sahel rainfall trends in the CMIP5 archive. *J. Geophys. Res. Atmos.*, **118**, 1613–1623, https://doi.org/10.1002/JGRD.50206.

——, 2019: Rainfall trends in the African Sahel: Characteristics, processes, and causes. *Wiley Interdiscip. Rev. Climate Change*, **10**, e591, https://doi.org/10.1002/WCC.591.

——, and A. Giannini, 2006: Robust Sahel drying in response to late 20th century forcings. *Geophys. Res. Lett.*, **33**, L11706, https://doi.org/10.1029/2006GL026067.

Bonfils, C. J. W., B. D. Santer, J. C. Fyfe, K. Marvel, T. J. Phillips, and S. R. H. Zimmerman, 2020: Human influence on joint changes in temperature, rainfall and continental aridity. *Nat. Climate Change*, **10**, 726–731, https://doi.org/10.1038/s41558-020-0821-1.

Braconnot, P., S. Joussaume, O. Marti, and N. de Noblet, 1999: Synergistic feedbacks from ocean and vegetation on the African monsoon response to mid-Holocene insolation. *Geophys. Res. Lett.*, **26**, 2481–2484, https://doi.org/10.1029/1999GL006047.

Caminade, C., and L. Terray, 2010: Twentieth century Sahel rainfall variability as simulated by the ARPEGE AGCM, and future changes. *Climate Dyn.*, **35**, 75–94, https://doi.org/10.1007/s00382-009-0545-4.

Charney, J. G., 1975: Dynamics of deserts and drought in the Sahel. *Quart. J. Roy. Meteor. Soc.*, **101**, 193–202, https://doi.org/10.1002/qj.49710142802.

Chen, M., P. Xie, and J. E. Janowiak, 2002: Global land precipitation: A 50-yr monthly analysis based on gauge observations. *J. Hydrometeor.*, **3**, 249–266, https://doi.org/10.1175/1525-7541(2002)003<0249:GLPAYM>2.0.CO;2.

Collins, J. W., and Coauthors, 2017: AerChemMIP: Quantifying the effects of chemistry and aerosols in CMIP6. *Geosci. Model Dev.*, **10**, 585–607, https://doi.org/10.5194/gmd-10-585-2017.

Dai, A., P. J. Lamb, K. E. Trenberth, M. Hulme, P. D. Jones, and P. Xie, 2004: The recent Sahel drought is real. *Int. J. Climatol.*, **24**, 1323–1331, https://doi.org/10.1002/joc.1083.

Deser, C., and Coauthors, 2020: Isolating the evolving contributions of anthropogenic aerosols and greenhouse gases: A new CESM1 large ensemble community resource. *J. Climate*, **33**, 7835–7858, https://doi.org/10.1175/JCLI-D-20-0123.1.

Dong, B., and R. Sutton, 2015: Dominant role of greenhouse-gas forcing in the recovery of Sahel rainfall. *Nat. Climate Change*, **5**, 757–760, https://doi.org/10.1038/nclimate2664.

——, ——, E. Highwood, and L. Wilcox, 2014: The impacts of European and Asian anthropogenic sulfur dioxide emissions on Sahel rainfall. *J. Climate*, **27**, 7000–7017, https://doi.org/10.1175/JCLI-D-13-00769.1.

Dyer, E. L. E., D. B. A. Jones, R. Li, H. Sawaoka, and L. Mudryk, 2017: Sahel precipitation and regional teleconnections with the Indian Ocean. *J. Geophys. Res. Atmos.*, **122**, 5654–5676, https://doi.org/10.1002/2016JD026014.

Folland, C. K., T. N. Palmer, and D. E. Parker, 1986: Sahel rainfall and worldwide sea temperatures, 1901–85. *Nature*, **320**, 602–607, https://doi.org/10.1038/320602a0.

Gaetani, M., C. Flamant, S. Bastin, S. Janicot, C. Lavaysse, F. Hourdin, P. Braconnot, and S. Bony, 2017: West African monsoon dynamics and precipitation: The competition between global SST warming and CO_2 increase in CMIP5 idealized simulations. *Climate Dyn.*, **48**, 1353–1373, https://doi.org/10.1007/s00382-016-3146-z.

Ganguly, D., P. J. Rasch, H. Wang, and J. H. Yoon, 2012: Fast and slow responses of the South Asian monsoon system to anthropogenic aerosols. *Geophys. Res. Lett.*, **39**, L18804, https://doi.org/10.1029/2012GL053043.

Giannini, A., and A. Kaplan, 2019: The role of aerosols and greenhouse gases in Sahel drought and recovery. *Climatic Change*, **152**, 449–466, https://doi.org/10.1007/s10584-018-2341-9.

——, R. Saravanan, and P. Chang, 2003: Oceanic forcing of Sahel rainfall on interannual to interdecadal time scales. *Science*, **302**, 1027–1030, https://doi.org/10.1126/science.1089357.

——, M. Biasutti, I. M. Held, and A. H. Sobel, 2008: A global perspective on African climate. *Climatic Change*, **90**, 359–383, https://doi.org/10.1007/s10584-008-9396-y.

——, S. Salack, T. Lodoun, A. Ali, A. T. Gaye, and O. Ndiaye, 2013: A unifying view of climate change in the Sahel linking intra-seasonal, interannual and longer time scales. *Environ. Res. Lett.*, **8**, 024010, https://doi.org/10.1088/1748-9326/8/2/024010.

Gidden, M. J., and Coauthors, 2019: Global emissions pathways under different socioeconomic scenarios for use in CMIP6: A dataset of harmonized emissions trajectories through the end of the century. *Geosci. Model Dev.*, **12**, 1443–1475, https://doi.org/10.5194/gmd-12-1443-2019.

Held, I. M., T. L. Delworth, J. Lu, K. L. Findell, and T. R. Knutson, 2005: Simulation of Sahel drought in the 20th and 21st centuries. *Proc. Natl. Acad. Sci. USA*, **102**, 17 891–17 896, https://doi.org/10.1073/pnas.0509057102.

Hoerling, M., J. Hurrell, J. Eischeid, and A. Phillips, 2006: Detection and attribution of twentieth-century northern and southern African rainfall change. *J. Climate*, **19**, 3989–4008, https://doi.org/10.1175/JCLI3842.1.

Hua, W., A. Dai, L. Zhou, M. Qin, and H. Chen, 2019: An externally forced decadal rainfall seesaw pattern over the Sahel and southeast Amazon. *Geophys. Res. Lett.*, **46**, 923–932, https://doi.org/10.1029/2018GL081406.

Hurrell, J. W., J. J. Hack, D. Shea, J. M. Caron, and J. Rosinski, 2008: A new sea surface temperature and sea ice boundary dataset for the Community Atmosphere Model. *J. Climate*, **21**, 5145–5153, https://doi.org/10.1175/2008JCLI2292.1.

Hwang, Y. T., D. M. W. Frierson, and S. M. Kang, 2013: Anthropogenic sulfate aerosol and the southward shift of tropical precipitation in the late 20th century. *Geophys. Res. Lett.*, **40**, 2845–2850, https://doi.org/10.1002/grl.50502.

Kawase, H., M. Abe, Y. Yamada, T. Takemura, T. Yokohata, and T. Nozawa, 2010: Physical mechanism of long-term drying trend over tropical North Africa. *Geophys. Res. Lett.*, **37**, L09706, https://doi.org/10.1029/2010GL043038.

Kay, J. E., and Coauthors, 2015: The Community Earth System Model (CESM) large ensemble project: A community resource for studying climate change in the presence of internal climate variability. *Bull. Amer. Meteor. Soc.*, **96**, 1333–1349, https://doi.org/10.1175/BAMS-D-13-00255.1.

Kirchmeier-Young, M. C., F. W. Zwiers, and N. P. Gillett, 2017: Attribution of extreme events in Arctic sea ice extent. *J. Climate*, **30**, 553–571, https://doi.org/10.1175/JCLI-D-16-0412.1.

Kushner, P. J., and Coauthors, 2018: Canadian snow and sea ice: Assessment of snow, sea ice, and related climate processes in Canada's Earth system model and climate-prediction system. *Cryosphere*, **12**, 1137–1156, https://doi.org/10.5194/tc-12-1137-2018.

Lamb, P. J., 1978: Large-scale tropical Atlantic surface circulation patterns associated with sub-Saharan weather anomalies. *Tellus*, **30**, 240–251, https://doi.org/10.3402/tellusa.v30i3.10338.

Li, X., and M. Ting, 2017: Understanding the Asian summer monsoon response to greenhouse warming: The relative roles of direct radiative forcing and sea surface temperature change. *Climate Dyn.*, **49**, 2863–2880, https://doi.org/10.1007/s00382-016-3470-3.

——, ——, and D. E. Lee, 2018: Fast adjustments of the Asian summer monsoon to anthropogenic aerosols. *Geophys. Res. Lett.*, **45**, 1001–1010, https://doi.org/10.1002/2017GL076667.

Liu, X., and Coauthors, 2012: Toward a minimal representation of aerosols in climate models: Description and evaluation in the Community Atmosphere Model CAM5. *Geosci. Model Dev.*, **5**, 709–739, https://doi.org/10.5194/gmd-5-709-2012.

Lu, J., and T. L. Delworth, 2005: Oceanic forcing of the late 20th century Sahel drought. *Geophys. Res. Lett.*, **32**, L22706, https://doi.org/10.1029/2005GL023316.

Malavelle, F. F., and Coauthors, 2017: Strong constraints on aerosol–cloud interactions from volcanic eruptions. *Nature*, **546**, 485–491, https://doi.org/10.1038/422974.

McKinnon, K. A., and C. Deser, 2018: Internal variability and regional climate trends in an observational large ensemble. *J. Climate*, **31**, 6783–6802, https://doi.org/10.1175/JCLI-D-17-0901.1.

Mohino, E., S. Janicot, and J. Bader, 2011: Sahel rainfall and decadal to multi-decadal sea surface temperature variability. *Climate Dyn.*, **37**, 419–440, https://doi.org/10.1007/s00382-010-0867-2.

Monerie, P. A., E. Sanchez-Gomez, and J. Boé, 2017: On the range of future Sahel precipitation projections and the selection of a sub-sample of CMIP5 models for impact studies. *Climate Dyn.*, **48**, 2751–2770, https://doi.org/10.1007/s00382-016-3236-y.

Myhre, G., and Coauthors, 2013: Anthropogenic and natural radiative forcing. *Climate Change 2013: The Physical Science*

Basis, T. F. Stocker et al., Eds., Cambridge University Press, 659–740.

Neale, R. B., and Coauthors, 2012: Description of the NCAR Community Atmosphere Model (CAM 5.0). NCAR Tech. Note NCAR/TN-486+STR, 274 pp., www.cesm.ucar.edu/models/cesm1.0/cam/docs/description/cam5_desc.pdf.

Oudar, T., P. J. Kushner, J. C. Fyfe, and M. Sigmond, 2018: No impact of anthropogenic aerosols on early 21st century global temperature trends in a large initial-condition ensemble. *Geophys. Res. Lett.*, **45**, 9245–9252, https://doi.org/10.1029/2018GL078841.

Palmer, T. N., 1986: Influence of the Atlantic, Pacific and Indian Oceans on Sahel rainfall. *Nature*, **322**, 251–253, https://doi.org/10.1038/322251a0.

Pausata, F. S. R., G. Messori, and Q. Zhang, 2016: Impacts of dust reduction on the northward expansion of the African monsoon during the Green Sahara period. *Earth Planet. Sci. Lett.*, **434**, 298–307, https://doi.org/10.1016/j.epsl.2015.11.049.

Pendergrass, A. G., D. B. Coleman, C. Deser, F. Lehner, N. Rosenbloom, and I. R. Simpson, 2019: Nonlinear response of extreme precipitation to warming in CESM1. *Geophys. Res. Lett.*, **46**, 10 551–10 560, https://doi.org/10.1029/2019GL084826.

Rayner, N. A., D. E. Parker, E. B. Horton, C. K. Folland, L. V. Alexander, D. P. Rowell, E. C. Kent, and A. Kaplan, 2003: Global analyses of sea surface temperature, sea ice, and night marine air temperature since the late nineteenth century. *J. Geophys. Res.*, **108**, 4407, https://doi.org/10.1029/2002JD002670.

Richardson, T. B., P. M. Forster, T. Andrews, and D. J. Parker, 2016: Understanding the rapid precipitation response to CO_2 and aerosol forcing on a regional scale. *J. Climate*, **29**, 583–594, https://doi.org/10.1175/JCLI-D-15-0174.1.

Rodríguez-Fonseca, B., and Coauthors, 2015: Variability and predictability of West African droughts: A review on the role of sea surface temperature anomalies. *J. Climate*, **28**, 4034–4060, https://doi.org/10.1175/JCLI-D-14-00130.1.

Rotstayn, L. D., and U. Lohmann, 2002: Tropical rainfall trends and the indirect aerosol effect. *J. Climate*, **15**, 2103–2116, https://doi.org/10.1175/1520-0442(2002)015<2103:TRTATI>2.0.CO;2.

Scaife, A. A., and Coauthors, 2009: The CLIVAR C20C project: Selected twentieth century climate events. *Climate Dyn.*, **33**, 603–614, https://doi.org/10.1007/s00382-008-0451-1.

Schneider, U., A. Becker, P. Finger, A. Meyer-Christoffer, B. Rudolf, and M. Ziese, 2015: GPCC full data reanalysis version 7.0 at 0.5°: Monthly land-surface precipitation from rain-gauges built on GTS-based and historic data, accessed 30 June 2017, https://doi.org/10.5676/DWD_GPCC/FD_M_V7_050.

Smith, S. J., J. Van Aardenne, Z. Klimont, R. J. Andres, A. Volke, and S. Delgado Arias, 2011: Anthropogenic sulfur dioxide emissions: 1850–2005. *Atmos. Chem. Phys.*, **11**, 1101–1116, https://doi.org/10.5194/acp-11-1101-2011.

Stone, D. A., and Coauthors, 2018: A basis set for exploration of sensitivity to prescribed ocean conditions for estimating human contributions to extreme weather in CAM5.1-1degree. *Wea. Climate Extremes*, **19**, 10–19, https://doi.org/10.1016/j.wace.2017.12.003.

Toll, V., M. Christensen, J. Quaas, and N. Bellouin, 2019: Weak average liquid-cloud-water response to anthropogenic aerosols. *Nature*, **572**, 51–55, https://doi.org/10.1038/s41586-019-1423-9.

Twomey, S., 1977: The influence of pollution on the shortwave albedo of clouds. *J. Atmos. Sci.*, **34**, 1149–1152, https://doi.org/10.1175/1520-0469(1977)034<1149:TIOPOT>2.0.CO;2.

Undorf, S., D. Polson, M. A. Bollasina, Y. Ming, A. Schurer, and G. C. Hegerl, 2018: Detectable impact of local and remote anthropogenic aerosols on the 20th century changes of West African and South Asian monsoon precipitation. *J. Geophys. Res. Atmos.*, **123**, 4871–4889, https://doi.org/10.1029/2017JD027711.

University of East Anglia Climatic Research Unit, P. D. Jones, and I. C. Harris, 2013: CRU TS3.21: Climatic Research Unit (CRU) Time-Series (TS) version 3.21 of high resolution gridded data of month-by-month variation in climate (Jan. 1901– Dec. 2012). NCAS British Atmospheric Data Centre, accessed 7 October 2019, https://doi.org/10.5285/D0E1585D-3417-485F-87AE-4FCECF10A992.

von Salzen, K., and Coauthors, 2013: The Canadian Fourth Generation Atmospheric Global Climate Model (CanAM4). Part I: Representation of physical processes. *Atmos.–Ocean*, **51**, 104–125, https://doi.org/10.1080/07055900.2012.755610.

Wang, C., 2015: Anthropogenic aerosols and the distribution of past large-scale precipitation change. *Geophys. Res. Lett.*, **42**, 10 876–10 884, https://doi.org/10.1002/2015GL066416.

Westervelt, D. M., and Coauthors, 2017: Multimodel precipitation responses to removal of U.S. sulfur dioxide emissions. *J. Geophys. Res. Atmos.*, **122**, 5024–5038, https://doi.org/10.1002/2017JD026756.

Willmott, C. J., and K. Matsuura, 2001: Terrestrial air temperature and precipitation: Monthly and annual time series (1950–1999) version 1.02, accessed 7 October, 2019, http://climate.geog.udel.edu/~climate/html_pages/README.ghcn_ts2.html.

Zelinka, M. D., T. Andrews, P. M. Forster, and K. E. Taylor, 2014: Quantifying components of aerosol–cloud–radiation interactions in climate models. *J. Geophys. Res. Atmos.*, **119**, 7599–7615, https://doi.org/10.1002/2014JD021710.